Journal of
Materials Chemistry C

Accepted Manuscript

This article can be cited before page numbers have been issued, to do this please use: H. Fan, Z. Fan, P. Li, F. Zhang, G. Tian, J. Yao, Z. Li, X. Song, D. Chen, B. Han, M. Zeng, S. wu, Z. Zhang, M. qin, X. Lu, J. Gao, Z. Lu, Z. Zhang, J. Dai, X. Gao and J.M. Liu, *J. Mater. Chem. C*, 2017, DOI: 10.1039/C6TC04615K.

ROYAL SOCIETY OF CHEMISTRY

rsc.li/materials-c

View Article Online
DOI: 10.1039/C6TC04615K

Journal Name

ARTICLE

Large Electroresistance and Tunable Photovoltaic Properties in Ferroelectric Nanoscale Capacitors Based on Ultrathin Super-Tetragonal $BiFeO_3$ Films†

Received 00th January 20xx,
Accepted 00th January 20xx

DOI: 10.1039/x0xx00000x

www.rsc.org/

Hua Fan,[a] Zhen Fan,[a] Peilian Li,[a] Fengyuan Zhang,[a] Guo Tian,[a] Junxiang Yao,[a] Zhongwen Li,[a] Xiao Song,[a] Deyang Chen,[a] Bing Han,[a] Min Zeng,[a] Sujuan Wu,[a] Zhang Zhang,[a] Minghui Qin,[a] Xubing Lu,[a] Jinwei Gao,[a] Zengxing Lu,[b] Zhi Zhang,[c] Jiyan Dai,[c] Xingsen Gao,*[a] and Jun-Ming Liu*[b]

Ferroelectric nanocapacitors with simultaneously tunable resistance and photovoltaic effect have a great potential for realizing high-density non-volatile memories and multifunctional opto-electronic nanodevices. Here, using a polystyrene spheres template method, we developed well-ordered Au nanoelectrode arrays on super-tetragonal $BiFeO_3$ (T-BFO)/$La_{0.7}Sr_{0.3}MnO_3$ (LSMO) epitaxial thin films, forming the Au/T-BFO/LSMO nanocapacitors. The nanocapacitors exhibited switchable resistance states and photovoltaic responses, controllable by the ferroelectric polarization of T-BFO. Thanks to the giant polarization of T-BFO, both giant electroresistance (ON/OFF current ratio > 20000) and noticeable photovoltage (~0.4 V) were achieved in the Au/T-BFO/LSMO nanocapacitors. These results demonstrate that the T-BFO-based nanocapacitors are promising for applications in high-density memories with multiple routes for non-destructive readout, as well as other multifunctional nanodevices.

Introduction

Ferroelectric resistive memories have emerged as a competitive memory technology owning to their outstanding advantages of nondestructive readout compared with traditional ferroelectric memories.[1-3] There have been mainly two types of ferroelectric resistive memories, *i.e.*, ferroelectric tunnel junctions (FTJs) and ferroelectric diodes. In FTJs, the quantum mechanical tunneling current is modified by the change of asymmetric tunnel barriers controllable with the ferroelectric polarization.[4-6] The electroresistance effect in ferroelectric diodes, on the other hand, is realized through the polarization modulation of the Schottky barriers at the ferroelectric/electrode interfaces.[7-12] Besides the tunable resistance, another consequence of the potential barrier modulation by polarization in both FTJs and ferroelectric diodes is the switchable photovoltaic effect.[13-18] This provides an opportunity to obtain some novel multifunctionalities, *e.g.* electro-photon double modulation of photovoltaic effects and resistive switching behaviours.[15,16,18] It may also allow some novel photoelectric devices such as electrically written and optically read non-destructive memories, multistate data storage devices, electrically tunable photosensors, or even energy harvesting devices.

For applications in integrated devices, it is indispensable to achieve both large electroresistance and sizable photovotatic properties with a small operation voltage. There have been a considerable number of studies working on the switchable photovoltaic effect, mainly in ferroelectric diodes[15,19-22] and less in FTJs.[16] In terms of photovoltaic performance, the large bulk thickness of conventional ferroelectric diodes (~100 nm) leads to serious recombination of photo-generated carriers, limiting the output photocurrent.[23-25] Recently, Hu et al[16] reported a giant electroresistance (ON/OFF current ratio ~ 10^5) together with noticeable and electrically tunable photovoltaic behaviours in FTJs based on ultrathin Sm-$BiFeO_3$ (~3 nm) films on Nb-$SrTiO_3$ (NSTO) substrates, suggesting that using ultrathin ferroelectric films may be an effective way to improve the photovoltaic properties. Nonetheless, those FTJs require a large operation voltage (~16 V) for achieving remarkable electroresistance effect, and the photovoltaic voltage (~100 mV) was also rather small. Obviously, further efforts are still needed to enhance the photovoltaic performance and reduce the operation voltage for microelectronic applications.

[a] Institute for Advanced Materials (IAM) and Guangdong Provincial Key Laboratory of Quantum Engineering and Quantum Materials, South China Normal University, Guangzhou 510006, China
*Email: xingsengao@scnu.edu.cn
[b] Laboratory of Solid State Microstructures and Innovation Center of Advanced Microstructures, Nanjing University, 210093, China
*Email: liujm@nju.edu.cn
[c] Department of Applied Physics, Hong Kong Polytechnic University, Hong Kong, China

†Electronic Supplementary Information (ESI) available: Details for patterning of top nanoelectrodes by polystyrene spheres template method, photovoltaic properties for BFO nanocapacitors with different sizes, and interface Schottky barrier profiles at dark and under light illumination derived from the fitting of *I-V* curves. See DOI: 10.1039/x0xx00000x

View Article Online
DOI: 10.1039/C6TC04615K

To improve the device performance, the ultrathin super-tetragonal $BiFeO_3$ (T-BFO) (<10 nm) would be a highly preferred candidate. T-BFO is chosen as the active material due to its giant polarization (~150 μC/cm^2),[26,27] benefiting both to the electroresistance and photovoltaic effects. For example, T-BFO based FTJs with large On/OFF current ratios were demonstrated.[28] In addition, previous studies revealed many interesting photo-related properties of T-BFO, such as persistent photoconductivity,[29] strain-gradient enhanced photocurrent,[30] large elasto-optic effect, and reversible electrochromism.[31] As a large polarization may benefit to a big electric modulation of Schottkey barrier, an enhancement of photovoltaic voltage can also be expected (see ESI† for detailed analysis). On the other hand, the very small thickness of FTJs (<5 nm) certainly causes insufficient light absorption and thus the total amount of photo-generated carriers is low,[32] suggesting that an intermediate BFO thickness is more likely to achieve sizable photocurrent and photovoltage output. A demo along this line may be appreciated, but so far the photovoltaic properties of T-BFO have not been directly measured and reported. Therefore, a comprehensive study of both electroresistance and photovoltaic effects in T-BFO is of great interest. Furthermore, with the ever increasing demand for high integration and miniaturization in microelectronics, the ability to scale down the device unit area has become a critical issue, which has not been well explored.

In this paper, we constructed Au/T-BFO/$La_{0.7}Sr_{0.3}MnO_3$ (LSMO) ferroelectric diodes with an intermediate T-BFO thickness (5~10 nm). To fulfill high-density application,[6,11,33] well-ordered arrays of Au electrodes were prepared using the polystyrene spheres template method, forming an array of metal-oxide-metal solid state nanocapacitors, as shown in Fig. 1a&b. We then investigated the electroresistance and photovoltaic effects in those nanocapicitors. A high electroresistance ratio (>20000) was obtained, thanks to the polarization modulated interface Schottky barriers. Meanwhile, an enhanced photovoltage could even reach 0.4 V, which is a rather high value achieved in ultrathin ferroelectric

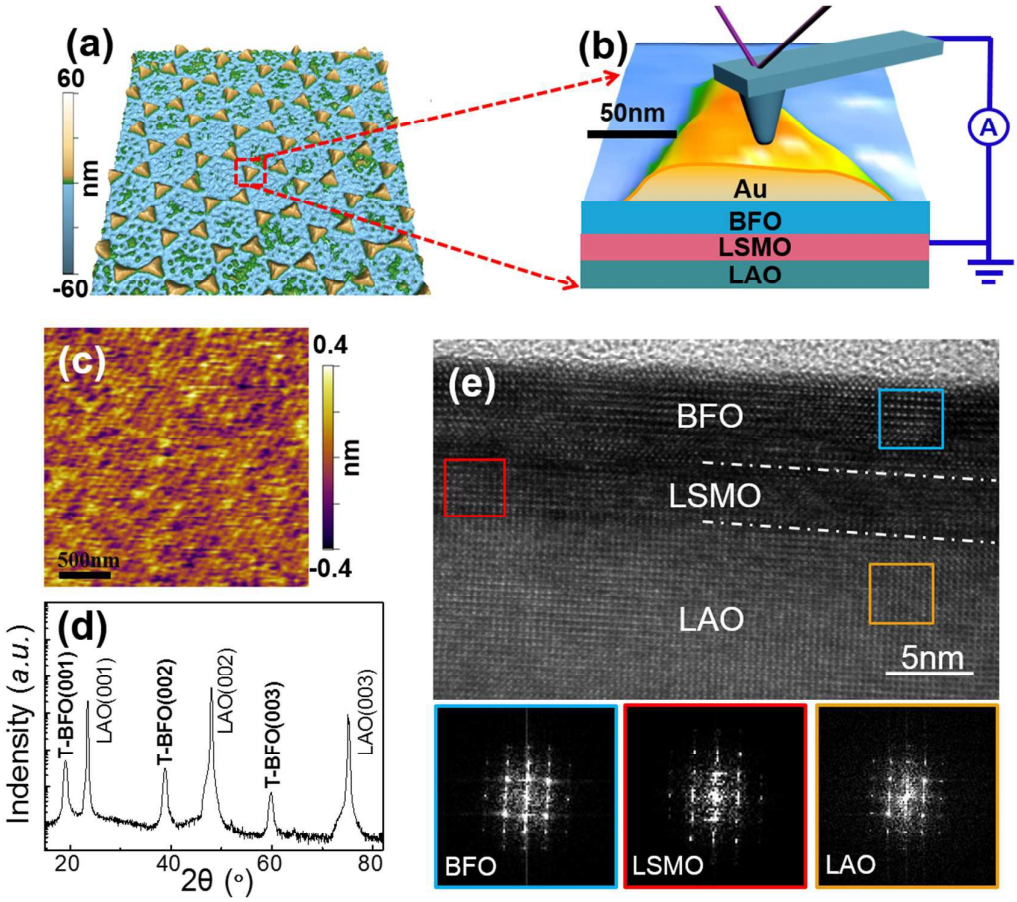

Fig. 1 Topographic images for the Au/BFO/LSMO nanocapacitors and microstructures for the constitution T-BFO film: (a) AFM image for the well-ordered array of Au/BFO/LSMO nanocapacitors. (b) Schematic of the set-up for I-V measurements on nanocapacitors through AFM tip. (c) AFM image of a BFO bare film (~8 nm). (d) X-ray diffraction θ-2θ scan of a thicker BFO film (30 nm) grown on LSMO/LAO substrates. (e) Cross-sectional TEM image of a BFO (5 nm)/LSMO/LAO heterostructure.

View Article Online
DOI: 10.1039/C6TC04615K

films below 10 nm. [16] In addition, notable optical modulated electroresistance and electrically controlled photovoltaic properties were also observed.

Experimental

Fabrication of well-ordered devices

The LSMO bottom electrodes were epitaxially grown on the $LaAlO_3$ (LAO) (001) substrates by pulsed laser deposition (PLD) using a KrF excimer laser (λ=248 nm) at a temperature of 670 °C and an oxygen pressure of 15 Pa. The BFO layers were subsequently grown at 660 °C with the same oxygen pressure. Well-ordered polystyrene spheres (diameter=500 nm) were then used as templates to fabricate Au nanoelectrodes. The detailed fabrication process is schematically shown in Fig. S1, ESI†.

Structure and morphology characterizations

The crystal structures of BFO films were characterized by X-ray diffraction (PANalytical X'Pert PRO). The microstructures were further examined by transmission electron microscopy (TEM: JEM-2100F, operating at 200 kV). The topography images were taken by atomic force microscopy (AFM, Cypher Asylum Research).

Electric and current characterizations

Piezoresponse force microscopy (PFM) and current atomic force microscopy (C-AFM) were conducted by a scanning probe microscopy (Cypher Asylum research) using Pt/Ir coated AFM probes (EFM-Arrow, nanoworld). The *I-V* curve, fatigue, and retention tests were conducted using C-AFM, by locating the AFM tip on the nano-sized top electrode of an individual nanocapacitor. The photovoltaic properties were obtained by introducing an ultraviolet light beam (wavelength λ = 365 nm) into the SPM sample stage connected with a Keithley source meter (Keithley, 6430).

Results and Discussion

The topography of Au/BFO/LSMO nanocapacitors is shown in Fig. 1a&b. As seen in Fig. 1b, the lateral area of a single nanocapacitor is about 0.01 μm^2. The topography of an 8-nm BFO bare film (Fig. 1c) shows an atomically flat surface with clear terraces and a roughness of only ~0.2 nm. To gain the structural information of the BFO layer, X-ray diffraction (XRD) was performed for a thicker BFO film (30 nm) grown on the LSMO-buffered $LaAlO_3$ (001) substrate, and the resulting XRD pattern is shown in Fig. 1d. The reflections from BFO (001), (002), and (003) planes can be well identified along with those from the LAO substrate. No impurities, foreign phases, or orientations other than (00l) reflections can be found. The c-axis lattice constant of BFO is calculated as 4.62Å, indicating a super-tetragonal (T) phase of BFO. It is deducible that the BFO films thinner than 30 nm also exhibit the T-phase due to the strain effect.[34] To verify it, the BFO (5nm)/LSMO/LAO heterostructure was examined by cross-sectional TEM. The high-resolution TEM image in Fig. 1e demonstrates the high-quality epitaxy of both BFO and LSMO layers. According to the fast Fourier transform (FFT) patterns, the c/a ratio is calculated as ~1.21, further confirming the T phase of BFO.

To reveal the ferroelectric nature of the BFO films, piezoresponse force microscopy (PFM) was conducted to record the local hysteresis loops and domain switching images after the electric poling. Fig. 2a shows the phase loop with 180° switching and the butterfly-like amplitude loop. Fig. 2b shows the out-of-plane PFM phase image of BFO domains after the poling with ±4 V. The distinct phase contrasts suggest that the BFO domains are respectively switched into two opposite orientations. These results thus demonstrate the ferroelectricity in the 8-nm T-BFO films. The C-AFM image after the poling is shown in Fig. 2c. The +4 V poled region (*i.e.*, polarization down) shows remarkably larger current than that of the -4 V poled region (*i.e.*, polarization up), suggesting a polarization dependent resistive switching (RS) behaviour.

To further study the conduction behaviours of the nanocapacitors, local current-voltage (*I-V*) characteristics were measured by the C-AFM on Au top electrodes (see the schematic set-up in Fig. 1b). The DC voltage sweeping frequency was 0.1 Hz (0.005 Hz for the measurement using Keithley 6430 for verification), and therefore the *I-V*

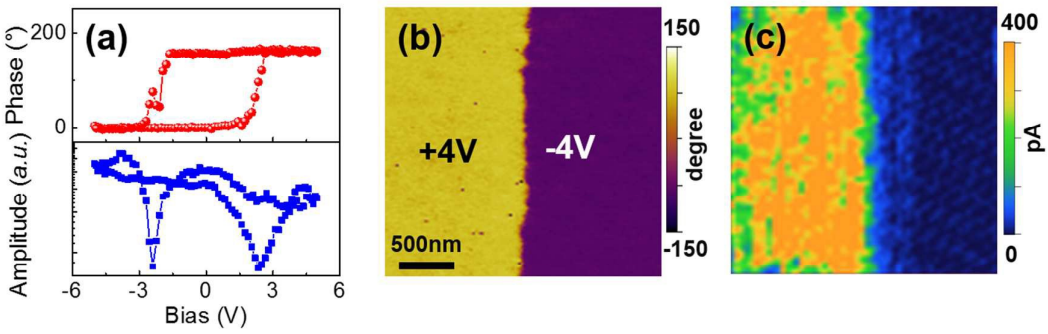

Fig. 2 Local piezoelectric and conductive properties for the 8-nm T-BFO films: (a) Local PFM hysteresis loops: phase signals (red) and amplitude signals (blue). (b) PFM out-of-plane phase image and (c) C-AFM image after poling with ±4 V (read at a scanning voltage of 1.5V).

View Article Online
DOI: 10.1039/C6TC04615K

measurements may be regarded as quasi-static ones. The voltage was applied through the tip (Pt/Ir) on the top electrodes, while the bottom electrode was grounded. The current compliance was set to be 20 nA. The sequence of voltage sweeping was: starting from 0 V, sweeping to -6 V and then back to +6 V, and eventually returning back to 0 V. We define a current to be positive if it flows from the top electrode to bottom one.

Fig. 3a presents the DC *I-V* characteristics of the nanocapacitors. The *I-V* curves for both capacitors based on T-BFO and rhombohedral BFO (R-BFO) show typical switchable diode behaviour. A broad hysteresis was observed for the T-BFO based nanocapacitor (upper panel), particularly in the positive voltage regime, indicating a significant change of resistance. This significant change is believed to be associated with the modulation of interface Schottky barrier by the polarization of T-BFO, as simulated by the conduction model of Schottky emission (see Fig. S2, ESI†). For a comparison, nanocapacitors based on R-BFO were tested too where the identical top (Au) and bottom (LSMO) electrodes were used, and the thickness of R-BFO was also 8 nm. As shown in Fig. 3a, the *I-V* hysteresis of the R-BFO based nanocapacitors (lower panel) is much slimmer than that of the T-BFO based nanocapacitors. This is consistent with the fact that the T-BFO has a larger polarization than the R-BFO.

The switchable diode effect observed in the T-BFO films with a thickness as small as 8 nm deserves further investigations,

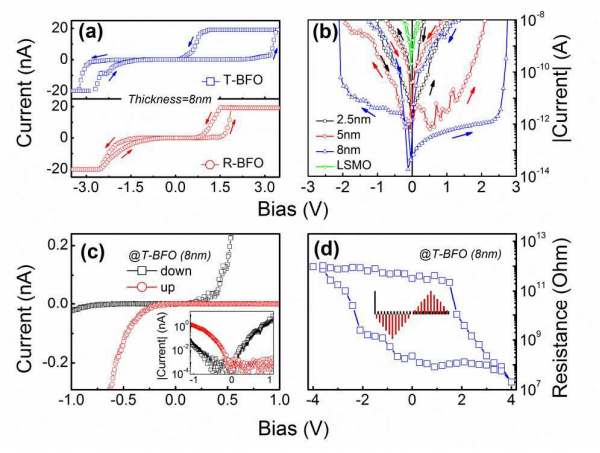

Fig. 3 Resistive switching properties for the Au/ BFO/LSMO nanocapacitors: (a) Comparison of *I-V* characteristics between T-BFO (8nm)/LSMO (5nm)/LAO (blue colour, upper panel) and R-BFO (8nm)/LSMO (5nm)/STO (red colour, lower panel) heterostructures. (b) *I-V* characteristics of nanocapacitors with different BFO layer thicknesses of 2.5 nm (black colour), 5 nm (red colour) and 8 nm (blue colour). (c) Linear plot of *I-V* curves within ±1.2 V of Au/T-BFO (8nm)/LSMO/LAO heterostructures after poling down (black colour) and up (red colour). Inset shows semi-logarithmic plot of the I-V curves. (d) Typical memristive hysteresis of resistance obtained by varying the write pulse amplitude for an Au/T-BFO (8nm)/LSMO capacitor.

because other conduction mechanisms may not be negligible given such a small thickness. It is of necessity to investigate the BFO layer thickness dependent conduction behaviour. Figure 3b shows the *I-V* characteristics of nanocapacitors with different BFO thicknesses of 2.5, 5, and 8 nm. The *I-V* curve of the 2.5-nm film is crossed near zero bias, which is in sharp contrast to the non-crossing *I-V* curve of the 8-nm film and is a typical feature of FTJ. The *I-V* curve of the 2.5-nm can be further fitted to the classical model of direct quantum-mechanical tunnelling, as shown in Fig. S3, ESI†, indicating that conduction mechanism in the 2.5-nm film may be tunnelling. However, in the 5-nm film, it seems that the switchable diode-type conduction behaviour dominates over the FTJ behaviour. Our results therefore suggest that the conduction mechanisms in the T-BFO based nanocapacitors may change from Schottky emission to tunnelling as the BFO film thickness reduces from 8 to 2.5 nm. This finding is consistent with previous theoretical predictions.[8] We note that the conductions in ferroelectric thin films can be extremely complex, and therefore we cannot exclude other mechanisms that may also be involved into the conductions in our BFO nanocapacitors. Nevertheless, the proposed mechanisms based on the existing *I-V* data can explain the experimental observations satisfactorily. It is also worth noting that the ON/OFF current ratio for the 8-nm film is the largest among the three samples.

To consolidate our claim that the observed RS is associated with the polarization switching, pulse voltages in addition to the DC bias voltages were also used for poling. As shown in Fig. 3c, a +4 V pulse poling resulted in a diode-like *I-V* behaviour with the positive forward diode direction. Upon a -4 V pulse poling, the polarization was switched and consequently the forward diode direction was reversed. The results are consistent with those obtained from the DC voltage sweeping. In addition, by varying the pulse voltage amplitude, the hysteretic variation of resistance (read @ 1V) was observed, indicating a memristive behaviour (see Fig. 3d).The well-defined high and low resistance states were found, corresponding to the polarization upward and downward states, respectively. This provides another evidence for the polarization switching induced RS behaviour. Note that the ON/OFF current ratios in the above measurements are as high as 20000 (Fig. 3b&c). Such high ON/OFF current ratios are comparable to the values reported for both FTJs[5,15] and conventional ferroelectric diodes[9-11] with relatively thick ferroelectric layers.

In terms of the device performance of RS, the Au/T-BFO/LSMO nanocapacitors show good electroresistance reproducibility, fatigue, and retention properties. It was demonstrated that significant RS behaviour with similarly large ON/OFF current ratios could be reproduced in at least 25 different devices (Fig. 4a). The *I-V* curves after the DC voltage sweeping for 3800 cycles exhibit minor distortions in shape (Fig. 4b), indicating good fatigue properties. The good electroresistance fatigue properties can also be proved by the pulse measurements (±4V pulse for writing and +1 V for reading). As seen in Fig. 4c, the variations of the high and low resistance states during the 1000 read/write cycles are small.

View Article Online
DOI: 10.1039/C6TC04615K

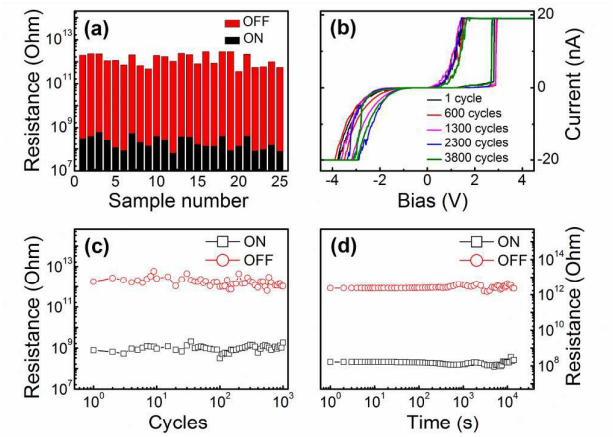

Fig. 4 Electroresistive performance of the Au/T-BFO (8nm)/LSMO nanocapcitors: (a) ON and OFF state resistances and corresponding ON/OFF current ratios of 25 different devices. (b) *I-V* curves after DC voltage sweeping for different cycles (up to 3800 cycles) for a selected device. (c) Fatigue properties of a typical nanocapacitor measured by pulse writing. (d) Retention properties measured up to 20000 seconds.

In the retention test, the high and low resistance states were considerably stable up to 10000 seconds (Fig. 4d). With the good RS performance and high density (2.5 Gbit/inch^2), the Au/T-BFO/LSMO nanocapacitor arrays are thus promising for high-density non-volatile memory applications. It is also worth mentioning that for our fatigue and retention tests, the nano-sized top electrodes were connected with the testing instruments through the small AFM probe, which inevitably brings about some vibration issues, making it difficult for a long test.

Besides the superior RS properties, the photovoltaic effect is also worth exploring because of the switchable diode effect controlled by the polarization of T-BFO. In our photovoltaic measurements, an Au electrode with a larger area of 1 μm^2 was used to enhance the photocurrent for easy detection. A laser source with ultraviolet light (wavelength λ = 365 nm) was used to illuminate the sample. The dark *I-V* curves in Fig. 5a demonstrate the switchable diode effect in the Au/T-BFO/LSMO heterostructures with the 1 μm^2 Au electrode. Fig. 5a also shows the clear evidence of photovoltaic behaviour in the Au/T-BFO/LSMO heterostructures after the negative poling, and the open-circuit voltage (V_{oc}) is ~0.4 V. However, after the positive poling, the enhancement of photoconductivity was observed while the V_{oc} was zero. The absence of photovoltaic behaviour in the polarization down state may be caused by the low built-in voltage related to the Schottky barriers. Before interpreting the origin of the photovoltaic effects, we show the light intensity dependent photovoltaic properties in Fig. 5b. As the light intensity increases, the V_{oc} increases slightly and the short-circuit current density (J_{sc}) increases much more significantly, which is a typical feature of the photovoltaic effect in ferroelectrics.[14]

Fig. 5c&d reveals the slow response of V_{oc} and rather fast response of J_{sc}. V_{oc} could reach 0.4 V, which is relatively high for ferroelectric films below 10 nm in thickness.[16] It is of interest to observe that upon the decrease of the lateral size of nanocapacitors, the V_{oc} rises significantly but the J_{sc} remains almost unchanged, as shown in Fig. S4, ESI†. This is probably due to the fact that less extrinsic leaking channels exist underneath electrodes with smaller sizes, favorable for a higher V_{oc}. In this connection, our nanocapacitors show advantages over conventional large-size capacitors in terms of high V_{oc}, which more likely reflects the intrinsic properties.

We now turn to the remaining question: how the switchable photovoltaic behaviour occurs in the heterostructures. From our analysis of the conduction behaviour, the *I-V* curves for the nanocapacitors can be well fitted with the Schottky emission model, and the details can be found in Fig. S5, ESI†. The schematic diagrams for the interface Schottky barrier profiles in both upward and downward polarization states are illustrated in Fig. 5e. For the upward polarization (pointing towards the Au/BFO interfaces), the barrier height at the BFO/LSMO and BFO/Au interfaces are Φ_L = 0.97 eV and Φ_R = 0.64 eV, respectively. The different barrier heights between the two interfaces also lead to an overall band bending of 0.33 eV, which is in associated with the built-in-voltage and

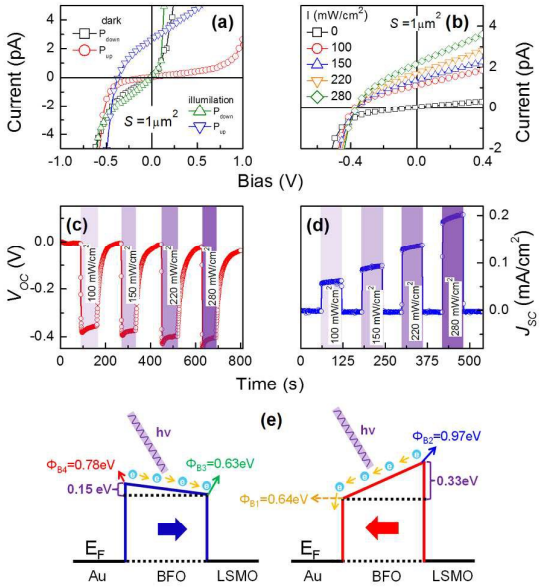

Fig. 5 Polarization modulated photovoltaic properties for an Au/T-BFO (8nm)/LSMO capacitor the 1-μm^2 Au electrode: (a) *I-V* curves measured under the conditions of dark and light illumination (λ=365 nm, 280 mW/cm^2). (b) Light intensity dependent photovoltaic *I-V* curves. (c) Open-circuit voltage V_{oc} and (d) Short-circuit current density J_{sc} as a function of time, when light was turned on and off alternatively during the measurement. (e) Schematic energy band diagrams of the capacitors under light illumination at polarization upward and downward states.

View Article Online
DOI: 10.1039/C6TC04615K

contributes to the separation of photo-generated charge carries contributing to the photocurrent and photovoltages. At the downward polarization state (pointing towards the BFO/LSMO interfaces), the band structure is greatly changed by the polarization state, leading to a different set of band profiles, with Φ_L = 0.63 eV, Φ_R = 0.78 eV, for BFO/LSMO and BFO/Au respectively. This produces a small overall built-in-voltage of -0.15 V. The different built-in-voltages (0.33V, and -0.15 V) are rather close to the observed photovoltaic voltages of 0.4 V and 0 V for the polarization upward and downward states, respectively, in spite of small deviations due to other factors, *e.g.* electron trapping or relaxation. Therefore it is confirmed that the observed switchable photovoltaic behaviour is caused by the polarization dependent Schottky barriers.

Fig. 6 shows both the optical modulation of resistive switching and the electric control of photovoltaic properties. Fig. 6a shows the *I-V* curves under different illumination intensities. It is found that the light illumination is able to apparently reduce the *HRS* resistance in the *I-V* curves but has little effect on the *LRS* resistance. This can be understood by that the amount of charge carriers in the *HRS* can be greatly increased by the photo-generated charge carriers, while they contribute little to the *LRS*. It is also noted that the light illumination can sizably reduce the onset voltages for the switching from *HRS* to *LRS*, which is likely due to the increase of charge carrier numbers or the change of the coercive of polarization switching, to be further addressed elsewhere. The modulation of the resistive properties under different light illumination intensities is summarized in Fig. 6b. It is indicated that with the increasing light intensity, the resistance in *HRS* monotonously decreases, while that in *LRS* remains nearly unchanged, producing a monotonous drop of ON/OFF current ratio against light intensity. With the increase of light intensity, the ON/OFF current ratio drops down from 10000 at dark to 2000 at 280 mW/cm^2, yielding a modulation ratio of nearly 5 times. Although the optical modulation of electroresistance is volatile, it may have potential applications in opto-electronic sensors. On the other hand, both the photovoltaic Jsc and V_{oc} can also be apparently modulated by electric pulsed voltages. The photocurrent (J_{sc}) and photovoltage (V_{oc}) as a function of pulse voltage are illustrated in Fig. 6c,d, both of which show hysteresis loops, indicating that the photovoltaic properties can be continuously controlled by electric pulses. As a result, we have obtained apparent photo-electric double control of electroresistance and photovoltaic properties in our devices. In particular, both the electroresitance and electric modulation of photovoltaic behaviour can be operated at low voltage pulses of 3~4V, much lower than the reported value (~16 V) in the FTJs.[16] These properties provide opportunities for many multifunctional devices such as opto-electronic sensors, photovoltaic readout non-destructive memories, or even energy harvesting devices. By the way, the additional interfacial effects such as interfacial spin and orbital coupling within the present structures may also be explored, which may lead to new multifunctional devices combining the optical, magnetic, and electrical properties.[35,36]

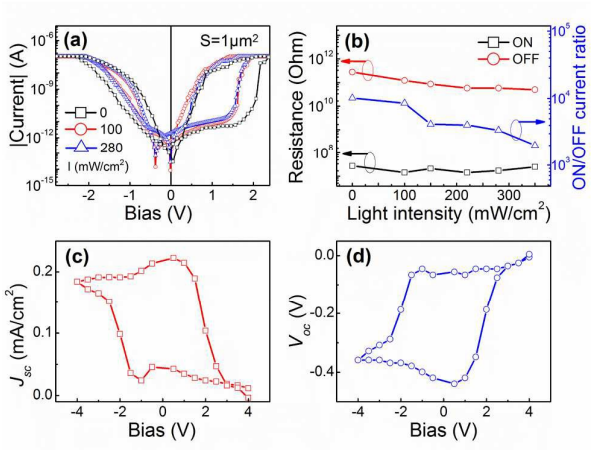

Fig. 6 Double modulation of electroresistance and photovoltaic effects for an Au/T-BFO (8nm)/LSMO nanocapacitor: (a) Resistive switching *I-V* curves under different light illumination intensities. (b) Resistances in *LRS*, *HRS*, and ON/OFF current ratio as a function of light illumination intensity. (c,d) Photovoltaic short circuit current J_{sc} (c) and open circuit voltage V_{oc} (d) as a function of pulse voltage under light intensity of 280 mW/cm^2.

Conclusions

To summarize, the high-density, well-ordered Au/T-BFO/LSMO nanocapacitor arrays were developed using the polystyrene spheres template method to deposit Au nanoelectrodes on the T-BFO/LSMO epitaxial thin films. The Au/T-BFO/LSMO nanocapacitors have a small lateral size and the T-BFO layer thickness is ~8 nm. These nanocapacitors exhibit switchable diode effect controlled by the polarization of T-BFO. As a result of the giant polarization, a large electroresistance (ON/OFF current ratio >10^4) and a noticeable and tunable photovoltaic voltage (~0.4 V) were achieved. Moreover, the double modulation of the electroresistance by light illumination and photovoltaic effect by electric pulses were also observed. The above results suggest that the T-BFO-based nanocapacitors are potentially useful for high-density non-volatile memories with non-destructive readout and multifunctional opto-electronic nanodevices.

Acknowledgements

The authors would like to thank the National Key Research Program of China (No. 1016YFA0201002), the State Key Program for Basic Researches of China (No. 2015CB921202), National Natural Science Foundation of China (No. 51272078, 51431006, 11674108, 51602110), the Project for Guangdong Province Universities and Colleges Pearl River Scholar Funded Scheme (2014), Science and Technology Planning Project of Guangdong Province (No. 2015B090927006), the Natural Science Foundation of Guangdong Province (No.

View Article Online
DOI: 10.1039/C6TC04615K

2016A030308019), and the International Science & Technology Cooperation Platform Program of Guangzhou (No. 2014J4500016). H. F. would like to thank the support by the Scientific Research Foundation of Graduate School of South China Normal University.

Notes and references

1 A. Chanthbouala, A. Crassous, V. Garcia, K. Bouzehouane, S. Fusil, X. Moya, J. Allibe, B. Dlubak, J. Grollier, S. Xavier, C. Deranlot, A. Moshar, R. Proksch, N. D. Mathur, M. Bibes, and A. Barthelemy, *Nat. Nanotechnol.*, 2012, **7**, 101-104.
2 V. Garcia, M. Bibes, *Nat. Commun.*, 2014, **5**, 4289.
3 S. Dong, J.-M. Liu, S.-W. Cheong, Z. F. Ren, *Adv. Phys.*, 2015, **64**, 519–626.
4 M. Y. Zhuravlev, R. F. Sabirianov, S. S. Jaswal, E. Y. Tsymbal, *Phys. Rev. Lett.*, 2005, **94**, 246802.
5 Z. Wen, C. Li, D. Wu, A. Li, N. Ming, *Nat. Mater.*, 2013, **12**, 617-621.
6 X. S. Gao, J.-M. Liu, K. Au, J. Y. Dai, *Appl. Phys. Lett.*, 2012, **101**,142905.
7 P. W. M. Blom, R. M. Wolf, J. F. M. Cillessen, M. P. C. M. Krijn, *Phys. Rev. Lett.*, 1994, **73**, 2107-2110.
8 D. Pantel, M. Alexe, *Phys. Rev. B*, 2010, **82**, 134105.
9 D. Pantel, S. Goetze, D. Hesse, M. Alexe, *ACS Nano*, 2011, **5**, 6032–6038.
10 A. Q. Jiang, C. Wang, K. J. Jin, X. B. Liu, J. F. Scott, C. S. Hwang, T. A. Tang, H. B. Lu, G. Z. Yang, *Adv. Mater.*, 2011, **23**, 1277–1281.
11 Z. X. Lu, Z. Fan, P. L. Li, H. Fan, G. Tian, X. Song, Z. W. Li, L. N. Zhao, K. R. Huang, F. Y. Zhang, Z. Zhang, M. Zeng, X. S. Gao, J. J. Feng, J. G. Wan, J.-M. Liu, *ACS Appl. Mater. Inter.*, 2016, **8**, 23963-23968.
12 C. Wang, K.-J. Jin, Z.-T. Xu, L. Wang, C. Ge, H.-B. Lu, H.-Z. Guo, M. He, G. Z. Yang, *Appl. Phys. Lett.*, 2011, **98**, 192901.
13 T. Choi, S. Lee, Y. J. Choi, V. Kiryukhin, S.-W. Cheong, *Science*, 2009, **324**, 63-66.
14 W. Ji, K. Yao, Y. C. Liang, *Adv. Mater.*, 2010, **22**, 1763–1766.
15 R. Guo, L. You, Y. Zhou, Z. S. Lim, X. Zou, L. Chen, R. Ramesh, J. Wang, *Nat. Commun.*, 2013, **4**, 1990.
16 J, W. Hu, Z. Wang, W. Yu, T. Wu, *Nat. Commun.*, 2016, **7**, 10808.
17 H. T. Yi, T. Choi, S. G. Choi, Y. S. Oh, S. W. Cheong, *Adv. Mater.*, 2011, **23**, 3403-3407.
18 L. Wang, K. J. Jin, C. Ge, C. Wang, H. Z. Guo, H. B. Lu, G. Z. Yang, *Appl. Phys. Lett.*, 2013, **102**, 252907.
19 R. Nechache, C. Harnagea, S. Li, L. Cardenas, W. Huang, J. Chakrabartty, F. Rosei, *Nat. Photonics*, 2014, **9**, 61-67.
20 H. Liu, J. Chen, Y. Ren, L. X. Zhang, Z. Pan, L. L. Fan, X. R. Xing, *Adv. Electron. Mater.*, 2015, **1**, 1400051.
21 Z. G. Xiao, Y. B. Yuan, Y. H. Shao, Q. Wang, D. F. Dong, C. Bi, P. Sharma, A. Gruverman, J. S. Huang, *Nat. Mater.*, 2015, **14**, 193-198.
22 L. F. Chen, Z. H. Cheng, W. T. Xu, X. J. Meng, G. L. Yuan. J-M. Liu. Z. G. Liu. *Sci. Rep.*, 2016, **6**, 19092.
23 M. Qin, K. Yao, Y. C. Liang, *Appl. Phys. Lett.*, 2008, **93**, 122904.
24 C. Paillard, X. F. Bai, I . C. Infante, M. Guennou, G. Geneste, M. Alexe, J. Kreisel, B. Dkhil, *Adv. Mater.*, 2016, **28**, 5153–5168.
25 P. Lopez-Varo, L. Bertoluzzi, J. Bisquert, M. Alexe, M. Coll, J. S. Huang, J. A. Jimenez-Tejada, T, Kirchartz, R. Nechache, F. Rosei, Y. B. Yuan, *Phys. Rep.*, 2016, **653**, 1-40.
26 D. Ricinschi, K. Y. Yun, M. Okuyama, *J. Phys.: Condens. Matter*, 2006, **18**, L97-L105.
27 Z. Fan, J. X. Xiao, H. J. Liu, P. Yang, Q. Q. Ke, W. Ji, K. Yao, K. P. Ong, K. Y. Zeng, J. Wang, *ACS Appl. Mater. Interfaces*, 2015, **7**, 2648−2653.
28 H. Yamada, V. Garcia, S. Fusil, S. Boyn, M. Marinova, A. Gloter, S. Xavier, J. Grollier, E. Jacquet, C. Carretero, C. Deranlot, M. Bibes, A. Barthelemy, *ACS Nano*, 2013, **7**, 5385-5390.
29 A. Bhatnagar, Y. H. Kim, D. Hesse, M. Alexe, *Nano lett.*, 2014, **14**, 5224-5228.
30 K. Chu, B. K. Jang, J. H. Sung, Y. A. Shin, E. S. Lee, K. Song, J. H. Lee, C. S. Woo, S. J. Kim, S. Y. Choi, T. Y. Koo, Y.-H. Kim, S.-H. Oh, M.-H. Jo, C.-H. Yang, *Nat. Nanotechnol.*, 2015, **10**, 972-979.
31 D. Sando, Y. Yang, E. Bousquet, C. Carretero, V. Garcia, S. Fusil, D. Dolfi, A. Barthelemy, P. Ghosez, L. Bellaiche, M. Bibes, *Nature commun.*, 2016, **7**, 10718.
32 Y. B. Yuan, Z. G. Xiao, B. Yang, J. S. Huang, *J. Mater. Chem. A*, 2014, **2**, 6027-6041.
33 L. N. Zhao, Z. X. Lu, F. Y. Zhang, G. Tian, X. Song, Z. W. Li, K. R. Huang, Z. Zhang, M. H. Qin, S. J. Wu, X. B. Lu, M. Zeng, X. S. Gao, J. Y. Dai, J.-M. Liu, *Sci. Rep.*, 2015, **5**, 9680.
34 R. J. Zeches, M. D. Rossell, J. X. Zhang, A. J. Hatt, Q. He, C.-H. Yang, A. Kumar, C. H. Wang, A. Melville, C. Adamo, G. Sheng, Y.-H. Chu, J. F. Ihlefeld, R. Erni, C. Ederer, V. Gopalan, L. Q. Chen, D. G. Schlom, N. A. Spaldin, L. W. Martin, R. Ramesh, *Science*, 2009, **326**, 977-980.
35 Y. W. Cao, X. R. Liu, P, Shafer, S. Middey, D. Meyers, M. Kareev, Z. C. Zhong, J. W. Kim, P. J. Ryan, E. Arenholz, J. Chakhalian, *npj Quant. Mater.*, 2016, **1**, 16009.
36 P. Jain, A. Stroppa, D. Nabok, A. Marino, A. Rubano, D. Paparo, M. Matsubara, H. Nakotte, M. Fiebig, S. Picozzi, E. S. Choi, A. K. Cheetham, C. Draxl, N. S. Dalal, V. S Zapf, *npj Quant. Mater.*, 2016, 1, 16012.

View Article Online
DOI: 10.1039/C6TC04615K

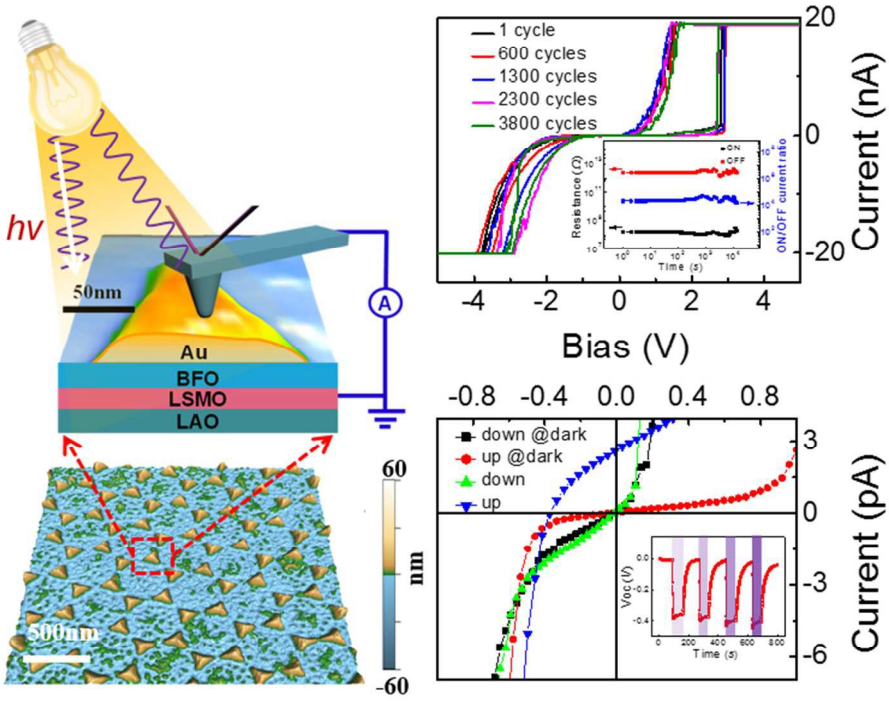

141x112mm (150 x 150 DPI)